Substrate-Independent Broad-Band Immersion Microlens Arrays with a High Coupling Efficiency for Infrared Focal Plane Arrays

Chang-Mo Kang, Simone Bianconi, Travis Hamilton, Jacob Rabinowitz, Skyler Wheaton, Lining Liu, Melville Ulmer, and Hooman Mohseni*

Cite This: https://doi.org/10.1021/acsaelm.2c00109 — Read Online

ACCESS | Metrics & More | Article Recommendations | Supporting Information

ABSTRACT: The sensitivity of infrared (IR) focal plane arrays (FPAs) is often limited by a low pixel fill factor. Solid immersion microlens arrays address this problem by focusing the light reaching each pixel into the most sensitive part of that pixel. This strategy is used in CMOS image sensors but has not been industrially adopted for IR FPAs due to significant difficulties in integration with compound semiconductors. Here, we present an all-in-one solution for producing solid immersion microlens arrays compatible with various IR FPAs regardless of their substrate material. Our strategy is to use refractive lenses made of SiO_2 and Si_3N_4 with very broad-band and efficient focusing abilities. Notably, our strategy works across a broad range of wavelengths with little performance degradation, meaning it is scalable to various applications. We implemented our method in short-wavelength IR FPAs and demonstrated 7.4 times improvement in quantum efficiency. This is the first demonstration of an immersion microlens array in a non-silicon infrared FPA.

KEYWORDS: short-wave infrared focal plane array (SWIR FPA), sensitivity, solid immersion microlens arrays, fabrication compatibility, broad-band light coupling, focusing efficiency
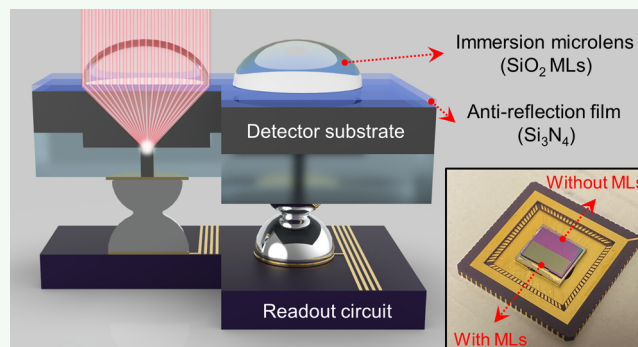
INTRODUCTION

In today's technological landscape, infrared (IR) cameras have become essential devices for observing and understanding various phenomena from the microscopic to the macroscopic world. They have found applications in a wide range of fields, including astronomy, biomedicine, military, and manufacturing.[1−3] As the range of applications grows, the demand is for IR cameras with increasingly high sensitivities. As an example, the field of exoplanet detection does not yet have an IR camera with the high-speed sensitivity needed to image Earth-like exoplanets in the habitable zone of distant stars.[4−6] Nonetheless, the sensitivity of IR imagers has not matched these demands despite intense research in this field.[7,8]

Most efforts toward increasing sensitivity revolve around the development of smaller photodetectors.[9−15] This follows from the definition of specific detectivity, a common metric of sensitivity,[16] as given by eq 1

$$D^* = \frac{\sqrt{A_o \text{BW}}}{\text{NEP}} \tag{1}$$

Here, A_o and BW are the optical area and bandwidth of a photodetector, respectively. NEP is the noise-equivalent power, defined as the ratio of the responsivity, R_I, and the noise current, I_n. By substituting the explicit expression for the responsivity and noise current, the specific detectivity can then be rearranged as[9]

$$D^* = \frac{\lambda}{hc} \eta \sqrt{\frac{1}{2(G+R)t} \cdot \frac{A_o}{A_e}} \tag{2}$$

where $\frac{hc}{\lambda}$ and η are the energy of the absorbed photons and the quantum efficiency of the detector, respectively. G and R are the excess carrier generation and recombination rates in the detector and A_e and A_o are the electrical and optical active areas, respectively. t is the thickness of the detector. From eq 2, it is evident that the sensitivity can be improved by scaling down the size of the detector's electronically active area (A_e) compared to its optically active area (A_o). Another source of enhanced sensitivity in smaller photodetectors is their lower internal capacitance, which is proven to enhance their overall sensitivity.[10] For these reasons, nanoscale and low-dimensional
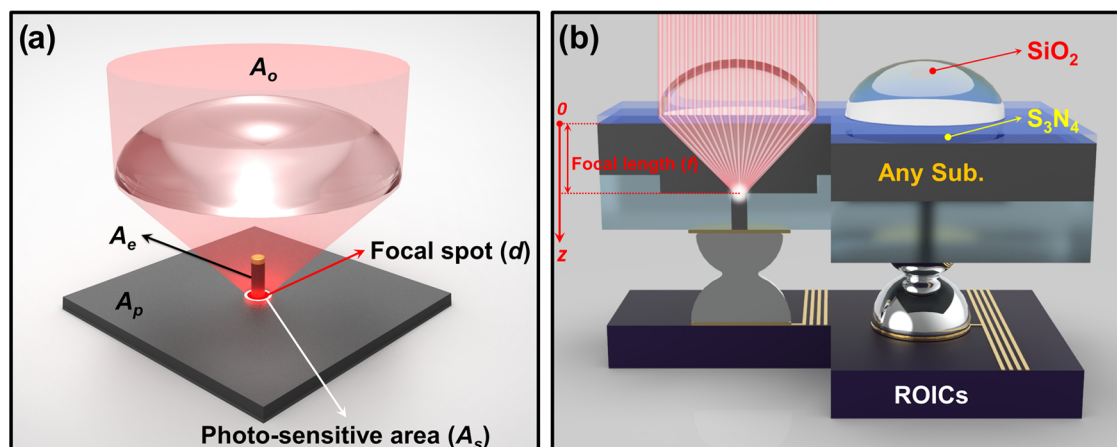
Figure 1. (a) Conceptual schematic showing that applying a light coupling system to LD photodetectors enables preservation of a large optical area by concentrating photons from an entire optical area (A_o) into the smaller photosensitive area (A_s). (b) Schematic of a SiO_2/Si_3N_4 immersion microlens array (MLA) integrated with IR FPAs based on LD photodetectors.

(LD) detectors such as quantum dots, nanowires, and two-dimensional materials have recently attracted increasing attention.[17−21] In some important applications, low-capacitance nanoscale detectors have already outperformed larger conventional detectors in terms of sensitivity and speed.[22]

Despite the promising performance reported for several LD detectors, most of them are still plagued by poor light coupling due to their small sizes, which limits their quantum efficiency.[9] Once utilized in an IR imager, these nanoscale photodetectors have a very small photosensitive area (A_s), representing a small fraction of the entire pixel area (A_p), and hence resulting in a low fill factor and quantum efficiency (η). To recover the full potential of LD photodetectors, incident light should be concentrated on the small A_s using a light coupling system. This is shown in the conceptual schematic of Figure 1a.

To achieve this effect, we have produced a solid immersion microlens array (MLA) directly on an IR focal plane array (FPA), which has been proven effective in conventional CMOS image sensors.[23,24] Nevertheless, current IR FPA technology still does not employ MLAs due to fabrication incompatibilities when working with CMOS and compound semiconductors. Section 1 of the Supporting Information details the research trends for applying MLAs to IR FPAs and their limitations. To date, most studies in MLAs applied to IR detectors have been limited to integration with a single detector of a large size.[11,25,26] An exception to this is represented by the case of PtSi FPAs based on Si substrates, which are easy to etch.[27] However, this approach is effective to only Si-based FPAs and thus not scalable to many mainstream IR FPAs consisting of compound semiconductors. To extend into various non-silicon IR FPAs, complex and expensive etching techniques must be separately developed for each substrate material, which is highly challenging, costly, and ineffective in some material systems. Therefore, IR MLA technologies that can provide a common solution for various substrates are highly sought-after. Recently, research on metasurface flat lenses has been conducted to address this issue, showing the potential for monolithic integration with various IR FPAs.[12] While the flat optics has attracted much attention and achieved interesting results when compared to the traditional refractive lens, the metasurface lenses still suffer from relatively poor focusing efficiency and are intrinsically limited to a narrow wavelength band operation.[28−30]

Here, we present an all-in-one MLA solution that is compatible with various types of IR FPAs regardless of the substrate material. This approach has the potential to achieve a high focusing efficiency for many small or LD devices across a broad range of wavelengths. Figure 1b shows a conceptual schematic of a solid immersion MLA integrated with IR FPAs based on LD photodetectors.

In this implementation, SiO_2 was chosen as the material for the refractive immersion MLA due to its broad-band transparency, wide etch selectivity, and ability to be deposited on any detector substrate (Figure 1b). Additionally, a Si_3N_4 layer was inserted between the SiO_2 MLA and the InP substrate to act as a broad-band antireflection coating. We performed a design-oriented numerical simulation of such MLAs to verify a good agreement with experimental characterizations of both the focusing and transmission properties of the MLAs in the short-wave infrared (SWIR) band. Most notably, we implemented the proposed MLAs on SWIR FPAs that we fabricated. To the best of our knowledge, this report presents the first successful demonstration of solid immersion MLAs on a non-silicon FPA that could be used for low-dimensional detectors made of different material systems.

■ RESULTS

Fabrication Compatibility and Focusing Efficiency. The focal length (f) of an immersion MLA is a very crucial optical parameter in determining the fabrication compatibility since it should be matched to the thickness of the detector's substrate (see Section 1 of the Supporting Information). To evaluate the range of focal lengths that can be obtained with the proposed MLA scheme, consisting of a SiO_2/Si_3N_4 (196 nm) multifilm stack, we performed a finite-difference time-domain (FDTD) simulation of electromagnetic wave propagation using a commercial software package (Lumerical). Details of the simulation conditions are shown in the Experimental Methods section. Here, the pixel pitch and the diameter of the MLA were set to 30 and 25 μm, respectively, to match the design of typical FPAs. For a fixed diameter, the desired focal length can be controlled by tuning only the sag, which is the height from the base of the lens to the highest point of the lens' surface. Here, the sag is used instead of the radius of curvature for controlling the focal length, as it is more convenient in terms of fabrication. The sag is expressed as eq 3
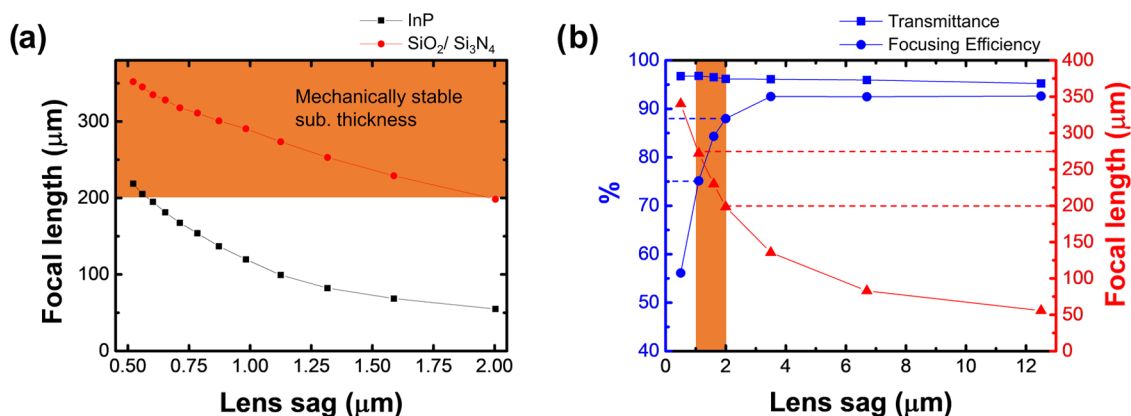
Figure 2. (a) Comparison of microlens focal lengths for SiO_2/Si_3N_4 (red circles) and InP (black squares) as a function of the lens sag. (b) Transmittances (blue squares), focusing efficiencies (blue circles), and focal lengths (red triangles) for SiO_2/Si_3N_4 as a function of its sag. This is for a lens with a diameter of 25 μm.
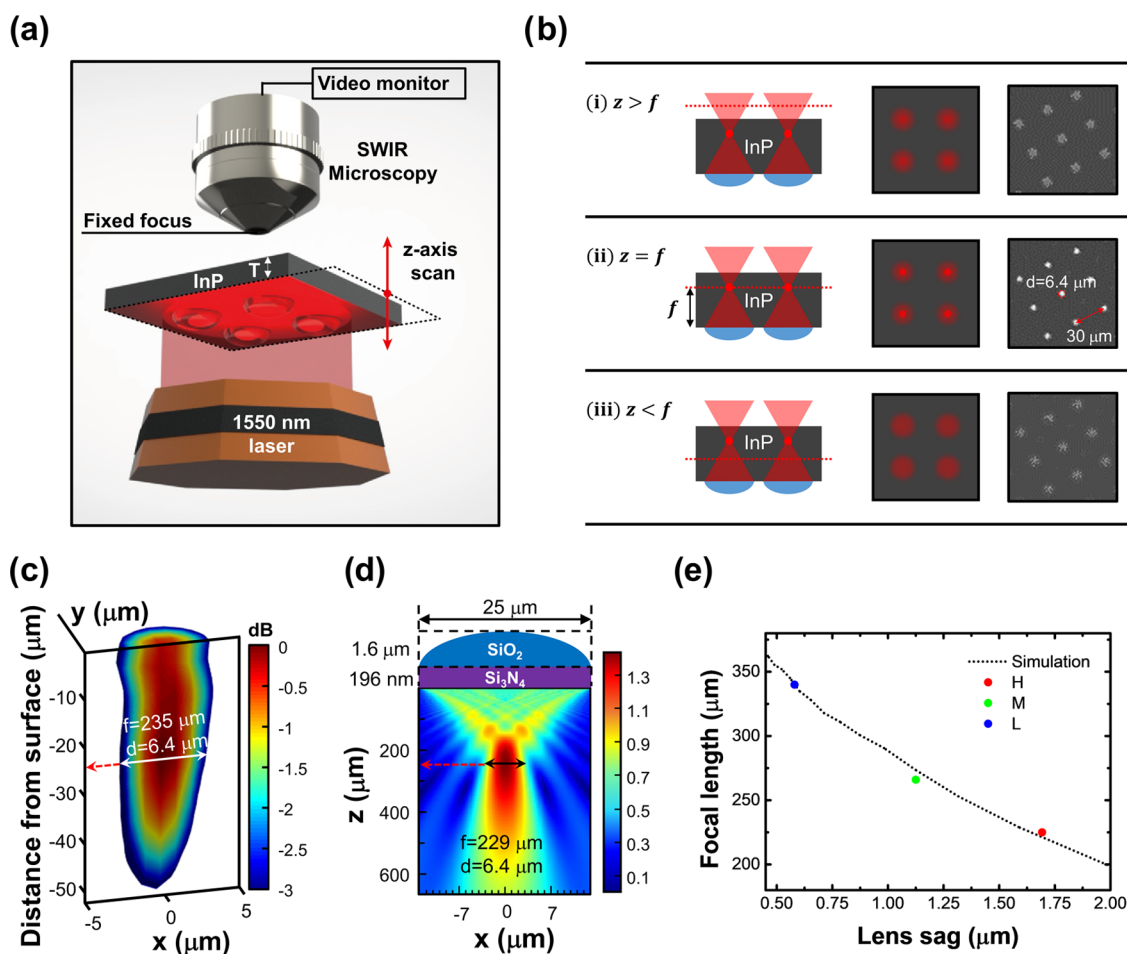

Figure 3. (a) Schematic of measurement setup and (b) method to measure the focal length: the red dashed lines represent the focusing plane of the three microscope images of focal spots obtained from the MLA (right). Here, a 1550 nm collimated beam was used. "z" is the distance between the substrate surface, where the MLA is located, and the focal plane of the microscope. (c) Cross-sectional three-dimensional (3D) plot of the measured focal intensities. (d) Simulated E-field intensity distribution of 1550 nm plane wave illumination onto a single microlens (SiO_2/Si_3N_4) with D = 25 μm and S = 1.6 μm. (e) Focal length plots obtained by simulation (black-dotted) and measured (circle points: "H", "M", and "L").

$$S = R - \sqrt{R^2 - \left(\frac{D}{2}\right)^2} \tag{3}$$

where R and D are the radius curvature and diameter of each microlens, respectively.

In Figure 2a, the focal length as a function of the lens sag for a SiO_2/Si_3N_4-based MLA and an InP-based MLA under 1550 nm plane wave illumination is shown. The focal length of SiO_2/Si_3N_4 lenses is much longer than that of InP-based lenses, thanks to the relatively low refractive index of SiO_2. Achieving focal lengths that are compatible with high-
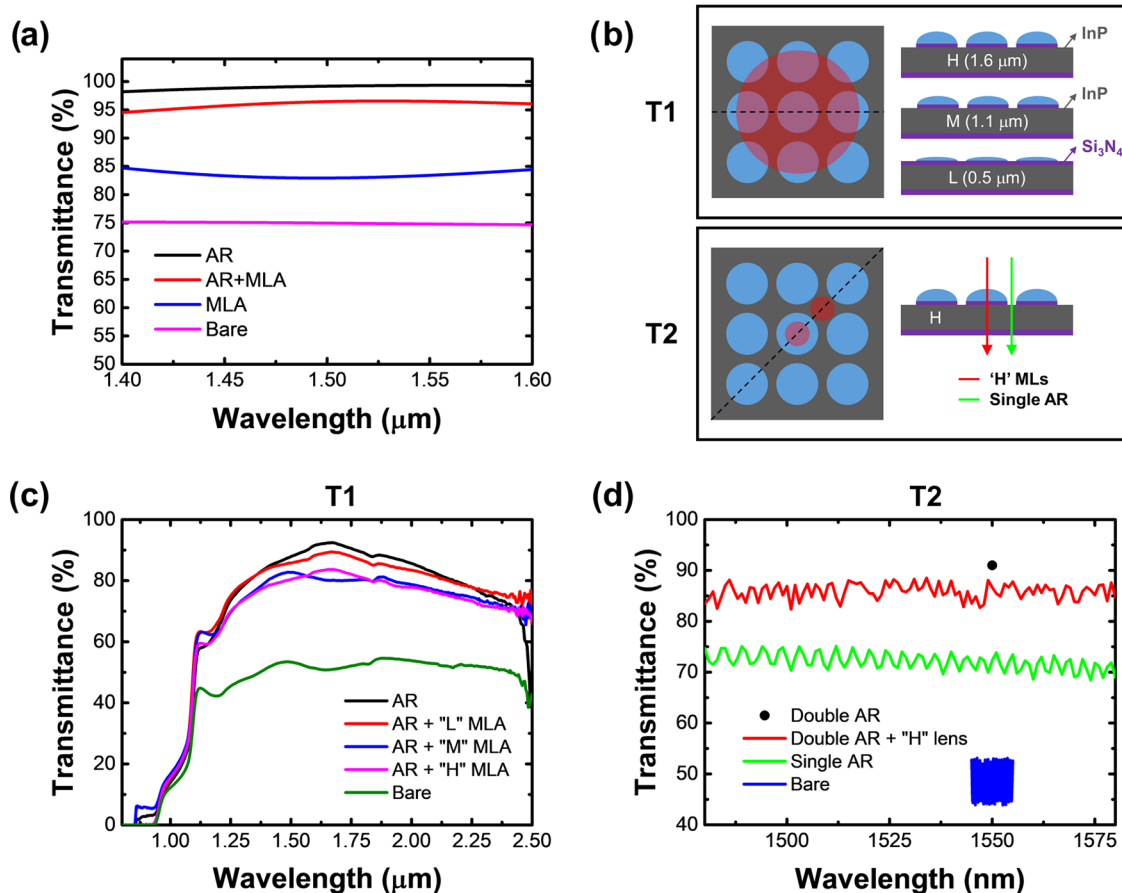
C

Figure 4. (a) Simulated transmittance of AR coating, AR+MLA, InP, and MLA. (b) Schematic for MLA transmittance measurement, which uses a laser beam spot larger than the microlens diameter ($T1$) and a low NA focused laser beam spot smaller than the microlens diameter ($T2$). The experimental transmittance results of (c) $T1$ and (d) $T2$ methods.

resolution FPAs is a crucial advantage of our method. In particular, the SiO$_2$/Si$_3$N$_4$ MLA allows using detector substrates above 200 μm thick, essential to ensuring reliable device fabrication, as shown in the orange-colored zone of Figure 2a. Additionally, SiO$_2$ enables thicker lenses, which are easy to fabricate compared to InP for a given focal length (i.e., substrate thickness). Using thicker lenses relaxes the constraints on etch selectivity and increases the repeatability and yield of the process. Section 2 in the Supporting Information numerically explains why thin InP MLAs are difficult to realize. Overall, these results imply that solid immersion MLA implementations can be more easily accomplished by employing low refractive index materials (n is 1.44 for SiO$_2$ and 1.99 for Si$_3$N$_4$ at λ = 1550 nm).

Focusing efficiency of the microlens is another crucial consideration. To investigate this, we simulated the focusing efficiency of a microlens and monitored the performance as the lens sag was varied. The focusing efficiency was calculated as the optical power (P_{out}) transmitted to the photosensitive area at the focus (-5 μm $\leq x, y \leq 5$ μm, $z = f$) divided by the input optical power (P_{source}) incident across the pixel pitch area (-15 μm $\leq x, y \leq 15$ μm, $z = 0$), as detailed in eq 4

$$\frac{P_{out}}{P_{source}} = \frac{\int_S \frac{1}{2} n \sqrt{\frac{\varepsilon_0}{\mu_0}} E_{xy}{}^2 (z = f) \, dx \, dy}{P_{source} \, (-15 \, \mu\text{m} \leq x, y \leq 15 \, \mu\text{m}, z = 0)} \quad (4)$$

where n, ε_0, μ_0, and $E_{xy}(z = f)$ are the refractive index of InP, vacuum permittivity, permeability, and the lateral electric field intensity distribution at the focus location, respectively.

As shown in Figure 2b, a larger sag (high numerical aperture (NA)) leads to higher focusing efficiency. In addition, the transmittance hardly reduces even with a thick sag. In short, MLAs with a larger sag will generally be preferred. Theoretically, a focusing efficiency of 90% or more can be achieved with a sag greater than 4 μm. However, there is a trade-off between fabrication compatibility and focusing efficiency. Typically, to achieve good coupling, the focal length of the MLA needs to be matched to the substrate thickness. Therefore, an MLA with a short focal length will require an FPA with a thin substrate. This imposes practical limits on the focal lengths that can be achieved with conventional processing and integration techniques. Therefore, it is necessary to find conditions that satisfy both manufacturing compatibility and high focusing efficiency when designing MLAs for integration with IR FPAs. In our experiments, we limited the focal length to 200 μm or more, which corresponds to MLA with a lens sag of 2 μm or less. We noted in our experiments and simulations that MLAs with a lens sag smaller than the target wavelength (i.e., less than 1 μm) do not effectively collect incident light. Considering the fabrication and performance limitations, the range of the recommended lens sag (orange zone in Figure 2b) is about 1–2 μm, which is similar to the size of the design target wavelength (λ = 1.55 μm). The corresponding range of
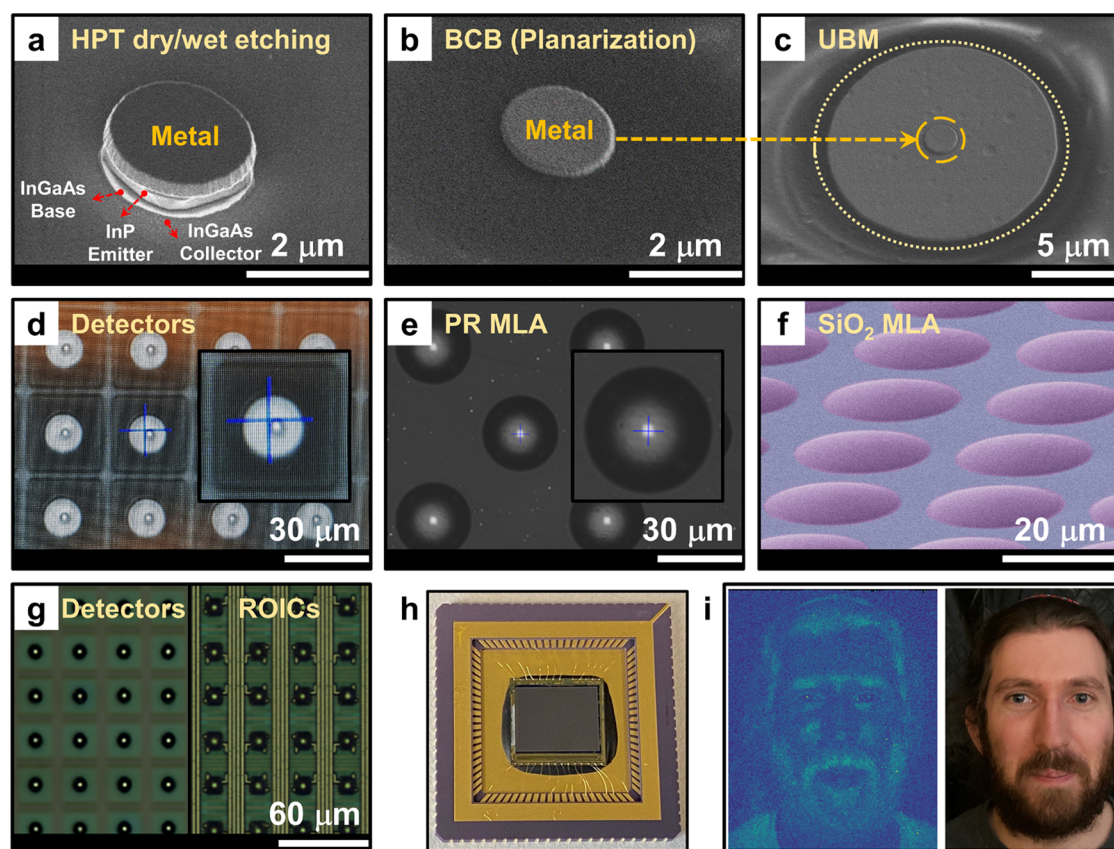
Figure 5. SEM images of (a) an HPT detector of 2 μm diameter, defined by the III−V material etching process, (b) a metal layer exposed after the BCB etch-back process, and (c) under-bump metal (UBM) layer connected with the detector metal electrode. Aligner microscope images showing alignment accuracy between (d) detectors and (e) reflowed resist lens arrays. (f) SEM image of a SiO$_2$ MLA (an MLA test sample was prepared ad-hoc on a Si bare wafer to avoid the possible damage and contamination of an actual FPA sample during these measurements.) (g) Microscope images of detector arrays and read-out integrated circuitry (ROIC) with indium bumps. (h) Uniform FPA device packaged by flip-chip bonding and wire bonding. (i) Face photo taken with the uniform SWIR imager (left) and a face photo taken with a smartphone camera (right) under the same illumination conditions.

the focusing efficiency in the recommended operation zone is 75−88%.

To experimentally validate the simulation results, we fabricated three MLA samples with different lens sags and measured their focal lengths using a 1550 nm collimated beam. For convenience, the three samples were denoted as 'L' (low: 0.5 μm), 'M' (medium: 1.1 μm), and 'H' (high: 1.6 μm), depending on their sag. Details on the fabrication and focal length measurements of the MLA samples are discussed in the Experimental Methods section (Figure 3a,b). Figure 3c shows a cross-sectional 3D beam intensity plot of the 'H' sample, which was obtained by grayscale pixel information extracted from a series of microscope images (Figure 3b). The measured focal length and beam spot size are 235 μm and 6.4 μm (4.13 λ), respectively (Figure 3c), both in good agreement with simulated values (Figure 3d). Similarly, the measured focal lengths of the "M" and "L" samples also agree with the focal lengths obtained from the FDTD simulations (Figure 3e). Among the three samples, the 'H' type lens had the brightest and smallest focal spots, as expected due to the lower F# (for 'L' and 'M', see Section 3 of the Supporting Information). In conclusion, we performed FDTD simulations on our proposed structures and matched the simulated results to experimental results with good agreement. This validation allows for the utilization of these simulations to estimate the optical

properties of various SiO$_2$/Si$_3$N$_4$ multifilm MLAs and guide the design of the MLAs for integration with SWIR FPAs.

Transmittance across SWIR. To ensure high quantum efficiency across the SWIR band, we need to minimize the optical loss caused by reflection. For InP ($n_{InP} \approx 3.16$ @ λ = 1.55 μm) surrounded by air (n_{air} = 1), the reflectance at normal incidence is estimated by the Fresnel equation to be about 27%, corresponding to a transmittance of 73%. The simulation results in Figure 4a show that the reflection at the InP interface can be naturally reduced even with just a SiO$_2$ MLA (T = 83% @ λ = 1.55 μm). By inserting the Si$_3$N$_4$ layer between the InP and SiO$_2$ MLA, the transmittance can be further enhanced up to 96% at λ = 1.55 μm, which is comparable to the transmittance of an ideal AR coating. To verify these simulation results, we measured the transmittances of bare InP (double polished), AR-coated InP (double coated), as well as of the 'H', 'M', and 'L' samples, via a conventional spectrophotometer equipped with a wide wavelength-tunable light source (0.8−2.5 μm) and an integrating sphere (T1 in Figure 4b). Since the spot size is much bigger than a single microlens, the fill factor of the microlens significantly affects its transmittance. In the 'H' and 'M' samples, the Si$_3$N$_4$ antireflection (AR) coating layer outside the MLA region was completely etched, while in the 'L' sample, it was not. The transmittance of the 'L' sample is about 87% at λ = 1.55 μm, and it is above 75% throughout a wide wavelength range
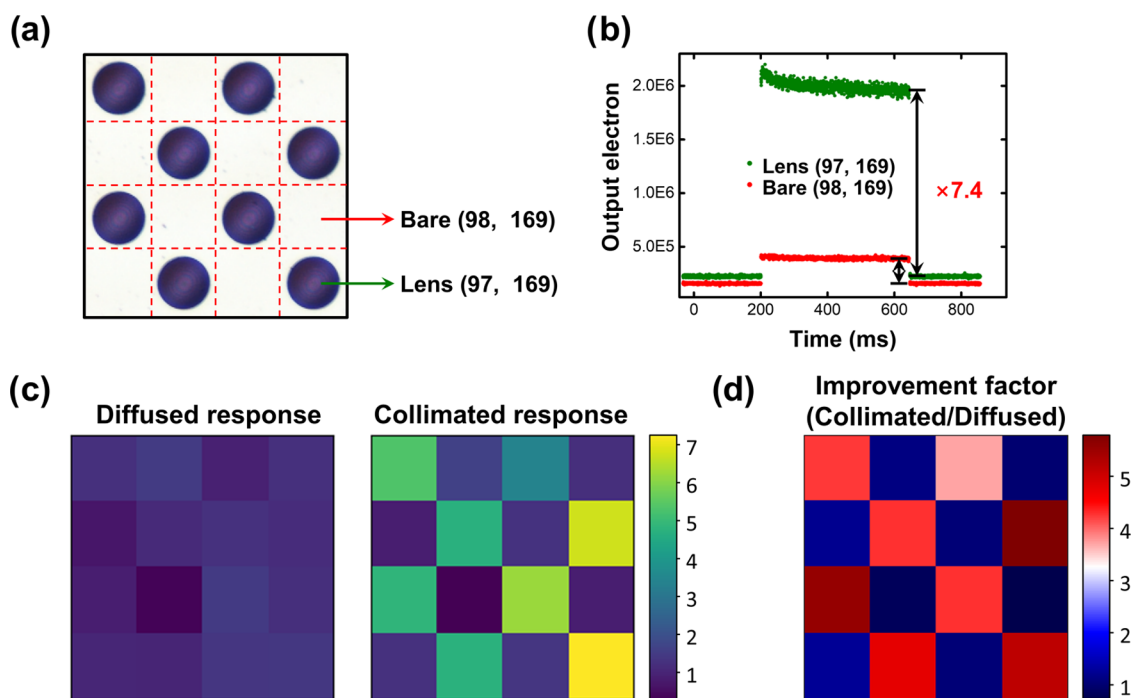
Figure 6. (a) Microscope image of the 'M' type MLA in a checkerboard pattern. (b) Bare (red) and lensed (green) pixels' raw output responses to a pulsed beam: the maximum measured enhancement is 7.4 times. (c) Response of a 4 × 4 pixel region to diffused (left) and collimated (right) illumination, normalized to the average response of bare pixels. (d) MLA improvement factor for the same pixel region: the improvement factors were obtained by dividing the collimated response by the diffused response. The maximum measured enhancement is about 7, and the average measured enhancement is about 5.

(1.25−2.5 μm) (Figure 4c). Meanwhile, the transmittances of 'M' and 'H' were lower than those of the 'L' sample: this difference is attributed to the fact that the 'M' and 'H' samples do not include any AR coating layer outside the microlens. Nevertheless, even these samples had a quite high transmittance across SWIR broad-band (>70% at 1.25−2.5 μm). To exclude the effect of the fill factor, we performed additional transmittance measurements using a laser beam focused on a spot smaller than the size of a microlens with a low NA, as shown in $T2$ of Figure 4b. The transmittance of the region outside a microlens ("H") is about 73% (at λ = 1.55 μm), which is identical to the results obtained by the Fresnel equation (Figure 4d). Meanwhile, the transmittance of the microlens is roughly 87% (at λ = 1.55 μm), showing a 15% enhancement in transmittance when compared to bare InP. The difference in transmittance between the microlens (87%) and AR samples (90%) is only 3%, which is in agreement with the simulation result (AR: 99%, AR + MLs: 96%). Furthermore, considering that the incident beam for the transmittance measurement must pass through both sides of the InP substrate unlike the IR FPAs and conceding some losses in the measurement due to high-angle scattering, the actual transmittance of the MLA is likely higher than 87% at λ = 1.55 μm. Although it is difficult to accurately measure the focusing efficiency experimentally, when considering the measured high transmittance (∼87%), small and bright focal spot (6.4 μm), and the above simulated high focusing efficiency (∼85%), it can be predicted that our MLAs have a high focusing efficiency of about 70−80%. From these results, we can confirm that our MLAs are ideal for applications with SWIR FPAs.

Compatible FPA Integration Process. After evaluating the characteristics of SiO_2/Si_3N_4 MLAs, we fabricated two

SWIR FPAs based on InGaAs/InP heterojunction phototransistors (HPTs) with integrated MLAs. One FPA was designed to check the performance difference with or without microlens by inserting the MLA in a checkerboard pattern, while the other FPA was designed to have a uniform MLA to check whether our strategy can guarantee yield and reliability. The epitaxial structure is detailed in our previous work.[22] The fabrication sequence is as follows: (i) detector array fabrication, (ii) MLA generation, and (iii) hybridization. The detailed procedures are explained in Section 4 of the Supporting Information.

The fabrication sequences were carefully designed to prevent performance degradation of the detector and MLA, by taking into account the effects of heat, mechanical pressure, and etching damages at each stage. For example, immediately following the detector array fabrication, a Si_3N_4 passivation layer was deposited onto the array to avoid possible damage and contamination of the detectors during the following processing steps, such as mechanical polishing or dry etching. To ensure process compatibility, all fabrication steps for the MLAs were conducted before read-out IC hybridization. The backside alignment accuracy between MLA and detector arrays was within 2 μm at the center of the array, as shown in Figure 5d,e. The alignment accuracy across the entire FPA is discussed in Section 5 of the Supporting Information. The surface morphology of the fabricated MLAs is smooth, as shown in the scanning electron microscopy (SEM) image in Figure 5f and the AFM image in Figure S5b. Moreover, the measured lens profile fits well with the designed radius of curvature, and the root-mean-square surface deviation is as small as 1.7% (see Figure S5c in Section 6 of the Supporting Information). It is also important to confirm the stability of the SiO_2/Si_3N_4 thin film since IR FPAs are typically operated at
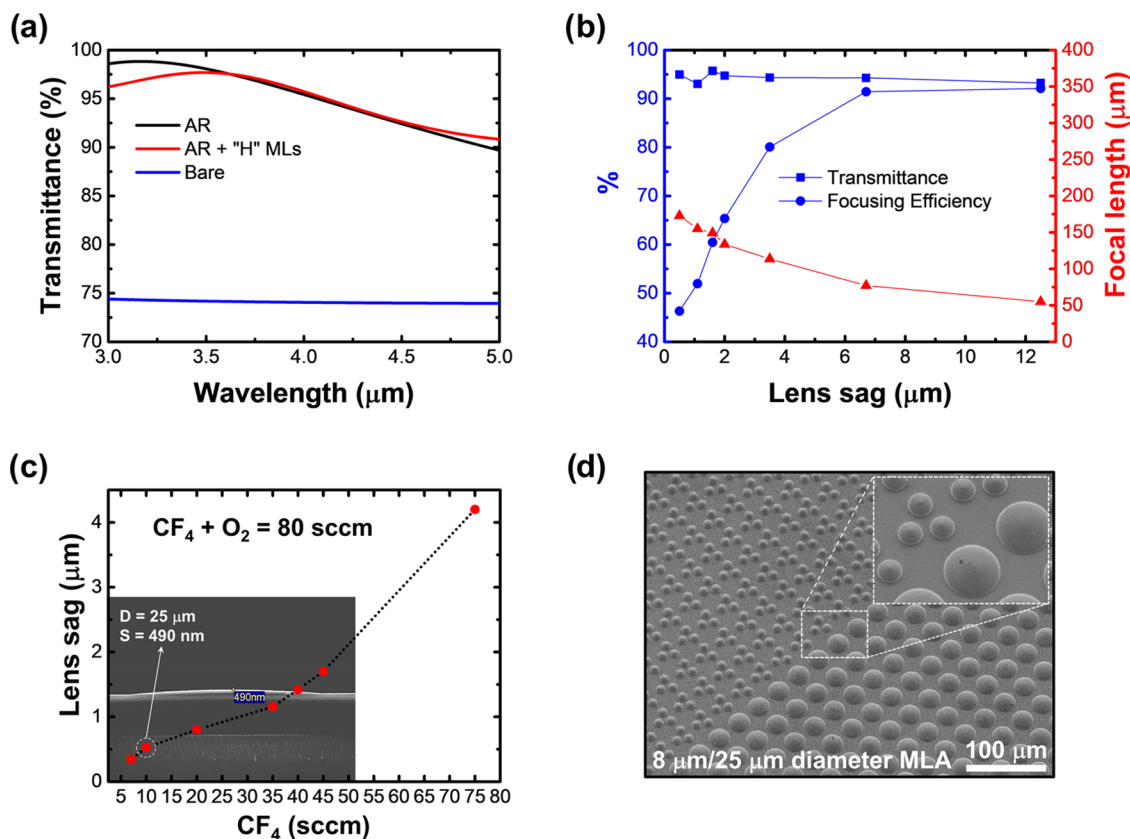
Figure 7. (a) Simulated transmittance of MLA, InP, and AR-coated samples in the MWIR band ($3-5$ μm). (b) Focal lengths and spot sizes simulated as a function of lens sag under a beam source with a center wavelength of 3.5 μm. (c) Etched depth of SiO_2 MLA under various gas mixing conditions. The inset shows the cross-sectional SEM image of a single microlens fabricated under CF_4/O_2 = 10/70 sccm gas conditions. The lens sag is about 490 nm. (d) Bird's eye view SEM image of an MLA with different diameters. The upper left and lower right regions include MLAs with 8 and 25 μm diameter, respectively.

low temperatures using the cooling system. The stacked thin film must survive for a long period without any cracks despite sudden temperature changes in a wide temperature range. No damage was found to the MLA after repeated cool-down cycles. After MLA fabrication, indium bumps were formed on the detectors and ROICs (Figure 5g), followed by chip dicing and flip-chip bonding. The flip-chip bonded sample was packaged to a chip carrier and wire-bonded for electrical connection to our camera measurement system (Figure 5h). To verify if our approach is compatible with the SWIR FPA fabrication, the heat map showing the respective pixel's operational responses (320 × 256 pixels) was obtained (Section 7 of the Supporting Information). Furthermore, we succeeded in imaging objects with the SWIR imager integrating with a uniform MLA. Figure 5i compares photographs of a face taken with the SWIR imager and with a smartphone camera under the same conditions. Considering that our device was fully manually fabricated into a chip scale, our strategy suggests that it can provide high reliability and operability. In addition, the noise and responsivity characterization shown in Section 8 of the Supporting Information confirmed that the lens formation process did not adversely affect the pixel performance. As a result, our approach allows MLAs to be manufactured on a wafer scale without performance degradation, enabling mass production of high-quality IR FPAs. Thanks to these advantages, we expect this study to provide crucial insights for the adoption of solid immersion MLAs in the IR FPA industry. A schematic of a

potential wafer-scale FPA fabrication flow is shown in Section 4 of the Supporting Information.

Lensed Pixel Measurement. The results presented in this work are from a fabricated SWIR FPA, which was designed to simultaneously include pixels both with and without microlenses to evaluate the effect of the MLA. Lenses were fabricated in a checkerboard pattern (Figure 6a). The sag and diameter of the fabricated lenses are the same as for the "M" sample mentioned above. Detailed camera measurements are explained in the Experimental Methods section. First, the photoresponses of two random adjacent pixels are compared in Figure 6b. The maximum measured output signal of the lensed pixel is increased by 7.4 times when compared to the pixel without a microlens. To more effectively separate the effect of the lenses from the intrinsic gain variation between pixels, we additionally characterized all pixels using diffused light. Since true diffused light (Lambertian) cannot be focused by a lens, it enables us to assess the performance of individual pixels without the effect of the lens. Figure 6c shows mapping images of the output response of 4 × 4 pixels obtained by heavily diffused illumination (left) and collimated illumination (right). Notably, under diffused illumination, the photoresponse of pixels with and without lenses is almost the same, and the checkerboard pattern is not observed. Conversely, the responses to the collimated beam clearly show the checkerboard pattern (right mapping image in Figure 6c), which corresponds with the design of the fabricated MLA pattern. The photoresponse of all lensed pixels is higher than that of

the bare pixels. To obtain the respective lens improvement factor, we normalized the collimated response to the diffused one: the results are shown in Figure 6d. The average measured improvement factor of the MLA was about five times, showing a significant improvement in the quantum efficiency of the detector thanks to the MLA. To the best of our knowledge, this is the first demonstration of solid immersion MLAs on SWIR FPAs.

Broad Applicability to Various IR FPAs. To ensure the compatibility of the proposed MLA implementation with various types of IR FPAs, it is necessary to first consider the optical properties of the MLA over a wide range of wavelengths. For this purpose, we used FDTD numerical simulations to investigate the optical properties of SiO_2/Si_3N_4 MLAs in the MWIR band (see Sections 9 and 10 of the Supporting Information for LWIR and MWIR, respectively). Since the refractive index of InP is close to that of the substrates used in many MWIR FPAs, the InP material was used as a substrate material in these simulations. The geometry of the simulated MLA was the same as that of the SWIR MLA, except for the thickness of the AR coating layer, which was increased to 400 nm. Interestingly, the MLA has transmittance above 90% across the MWIR broad-band (3−5 μm), showing great potential for MWIR FPAs (Figure 7a). Figure 7b shows the simulated focal lengths and focusing efficiency formed by such MLAs under λ = 3.5 μm collimated light sources from the simulation. The focusing efficiency of 80% or more can be achieved with a sag greater than 4 μm. However, when compared to the SWIR MLA, the focal length of the MWIR MLA is much shorter overall, and the focusing efficiency is lower under the same lens sag. In short, it means that the integration of the MWIR MLA is more challenging than that of the SWIR MLA. This short focal length for the lens operating in MWIR is primarily due to the relatively long target wavelength but not due to the difference in the lens material or approach; hence, this issue is intrinsic to most MWIR lenses. Despite the challenging design condition, our MLA strategy can be compatible with MWIR FPAs when using 1.6 μm of sag corresponding to a focal length of about 150 μm. At this focal length, the focusing efficiency is 63%, which is expected to be a practical and promising result. This is a noteworthy result in that it suggests that these MLAs can cover broad-band operations ranging from SWIR to MWIR.

In terms of manufacturing, for the MLA to be compatible with various substrates with different refractive indices, it is necessary to demonstrate the feasibility of a wide range of radii of curvature. For a fixed diameter of the microlens, the radius of curvature is determined by the sag of the lens. Thus, we tested various SiO_2 MLAs with different sags by tuning the CF_4/O_2 ratio during the RIE. As shown in Figure 7c, by simply changing the gas mixing ratio, we were able to reliably tune the MLA radius of curvatures over a range from 200 to 20 μm, corresponding to sags of 400 nm and 4 μm, respectively. Thanks to the wide etch selectivity of SiO_2, size scalability of these MLAs was also demonstrated: a fabricated MLA with a pixel pitch of less than 10 μm is shown in Figure 7d. Consequently, when considering optical properties and manufacturing comprehensively, our strategy has great potential to be extended into various IR FPAs based on different material systems and resolutions.

DISCUSSION

To maximize the sensitivity of IR FPAs, it is necessary to jointly optimize the performance of both the photodetectors and the MLA. As mentioned above, scaling down the size of the photodetectors reduces both the dark current and junction capacitance, which improves the sensitivity. However, this approach can also lead to a reduction in quantum efficiency due to relatively poor light coupling, which would hinder the detection performance. For this reason, including considerations on the size, weight, and power consumption (SWaP) of imagers, the optimal FPA design was found to correspond to diffraction-limited pixel sizes.[13,31] This size depends on the wavelength and detection materials of interest. Furthermore, the practical optimal detector size may be slightly larger to ease the constraint on diffraction-limited optics.

There are three methods to optimize the performance of MLAs to approach the fabrication of diffraction-limited imagers. The first is to lower the F# of the MLA by decreasing the thickness of the substrate. As discussed, in this study, the thickness of the InP substrate was limited to ensure stability during the fabrication (focal length: 280 μm), so MLAs with relatively high F#, and hence large spot size, were designed. However, a focal spot (d) larger than the pixel photosensitive region (A_s) can lead to optical loss in the nonsensitive area (see Figure 1a). Therefore, to minimize the area difference between A_s and d, it is crucial to find the minimum substrate thickness that retains stability through the entire fabrication process. For wafer-scale fabrication, a carrier substrate can be used to help provide stabilization during mechanical polishing, permitting further reduction of substrate thickness without compromising structural integrity.[32−34] Envisioning the development of thin wafer processing in the future, the optical characteristics of low F# lenses are simulated in Section 11 of the Supporting Information.

The second optimization method is to maximize the fill factor of the lenses, defined as $FF = \frac{A_o}{A_p}$ (see Figure 1a). In this study, we used the most accessible reflow method, and the FF was about 50%. When using a reflow method, a gap between the resist patterns is essential for the resist to transform into a lens-like shape, making this FF reduction inevitable.[35] For this reason, the higher the FPA resolution, the smaller the FF. Alternatively, the FF of the MLA can be improved by employing other reported methods such as hexagonally packed lens array[35] and grayscale photolithography.[36] As an example, the grayscale photolithography method, which enables the generation of lens-shaped resists without a reflow process, can help achieve a higher FF. In short, the presented strategy is not necessarily tied to the reflow method and the specific pattern array. Finally, the lensing can be further improved by implementing a more accurate alignment between the photosensitive region and focal spots. While our MLA showed a considerable improvement in FPA quantum efficiency by an average factor of 5, it is expected that the effect of the MLA can be even further improved if the MLA fabrication is optimized as discussed.

CONCLUSIONS

In summary, solid immersion MLAs are presented here as an avenue to boost the performance of the next generation of IR photodetectors based on small detector sizes and LD materials. We have experimentally and numerically demonstrated the

compatibility of SiO_2/Si_3N_4 immersion MLAs with various IR FPAs. The focal length of the MLA is applicable to various IR detector substrates, thanks to the low refractive index of SiO_2. The transmittance was found to be as high as 90% across a broad-band range from SWIR to MWIR. In addition to the evaluation of the lens itself, we characterized lensed pixel detectors from an actual SWIR FPA and demonstrated the quantum efficiency improvement thanks to the MLA. Most importantly, our strategy can be applied to various FPA platforms with high efficiency regardless of the detector substrate and resolution. We believe that our study will constitute a good reference for integrating MLAs on IR FPAs and represent a promising candidate as a standard process for IR solid immersion MLAs.

EXPERIMENTAL METHODS

MLA Fabrication. To replicate the simulation results, the backside of an InP bare wafer was polished to a mirror-like condition. A 196 nm thick Si_3N_4 AR coating layer was deposited on both sides of the wafer using plasma-enhanced chemical vapor deposition (PECVD). The wafer was then cleaved into three samples to fabricate different types of MLAs. After cleaning the samples thoroughly, three SiO_2 layers with different thicknesses (0.6, 1.2, and 1.8 μm) were deposited on one side of the respective samples by PECVD. To improve the surface adhesion between SiO_2 and the resist, hexamethyldisilazane was coated on the samples, followed by baking at 110 °C for 1 min. After baking, a spin coating of the AZ 4620 photoresist was applied to the sample surface. The photoresist thickness applied to all samples was approximately 7 μm. This layer stack yields a 30% resist aspect ratio, which is our optimized condition for obtaining high-quality lens-shaped resists. The samples were soft-baked at 110 °C for 1 min, followed by a 1 h rest for rehydration between soft bake and exposure. Using a photolithography aligner (maskless aligner 150), cylinder resists were patterned. The sample was baked at 130 °C for 2 min to reflow the cylinder resists into a lens shape. To ensure reliable etching control, the total gas flow of CF_4/O_2 was set to 80 sccm. For "L", "M", and "H", the CF_4/O_2 gas conditions were 10/70, 35/45, and 45/35 sccm, respectively. The RIE was then performed until all resists were removed so that the lens-shaped resist's curvature can be transferred to SiO_2.

Focal Length Measurement. Figure 3a shows a schematic of the optical setup for measuring the focal lengths of the fabricated samples. Each sample was mounted with the MLA facing downward on a motorized micropositioning stage that can scan in the z-axis with sub-μm accuracy. The top SWIR microscope was focused on the top of the substrate (i.e., the backside of the MLA), and a 1550 nm collimated beam was incident from the bottom (i.e., the front side of the MLA). A series of microscope images were captured while the MLA sample position was scanned along the z-axis. As shown in the conceptual schematic of Figure 3b, the focal length of the MLA was measured by finding a z-axis position with the maximum intensity of their focal spots.

Camera Measurement. To find the improvement factor due to the MLA, we first needed to compensate for the individual gains and fill factors of each of the photodetectors. The gains were found by measuring the detectors' responses to pulses of light produced by passing an expanding beam through several dispersive layers. This ensured that each detector saw a uniformly glowing screen, so that incident light arrived from all possible angles and was not relevantly focused by the microlenses. The MLA was arranged in a checkerboard pattern on the FPA, so each lensed pixel was adjacent to four bare pixels. These provided a local reference for how a bare detector responded to the same conditions that the lensed detectors experienced. The responses for both types of pixels were normalized by their respective gains to compensate for differences in fill factor between the pixels. The improvement factor was then calculated as the ratio of the lensed response to the bare response.

FDTD Simulation Condition.

- FDTD range: $[x] = [-15,\ 15\ \mu m]$, $[y] = [-15,\ 15\ \mu m]$, $z = [-400,\ 10\ \mu m]$
- Launch source type: Gaussian beam (NA = 0.059, λ = 1550 nm), grid size = $\frac{1}{15}\lambda$
- SiO_2 lens: diameter = 25 μm, n = 1.44
- Si_3N_4 layer: $[x] = [-15,\ 15\ \mu m]$, $[y] = [-15,\ 15\ \mu m]$, $z = [0, 0.196\ \mu m]$, n = 1.99
- InP substrate: $[x] = [-15,\ 15\ \mu m]$, $[y] = [-15,\ 15\ \mu m]$, $z = [-400\ \mu m,\ 0]$, n = 3.1649

ASSOCIATED CONTENT

ⓢ Supporting Information

The Supporting Information is available free of charge at https://pubs.acs.org/doi/10.1021/acsaelm.2c00109.

AUTHOR INFORMATION

Corresponding Author

Hooman Mohseni — *Department of Electrical and Computer Engineering, Northwestern University, Evanston, Illinois 60208-2900, United States; Department of Physics & Astronomy and CIERA, Northwestern University, Evanston, Illinois 60208-2900, United States;* ⓞ orcid.org/0000-0002-0183-4213; Phone: (847) 491-7108; Email: hmohseni@northwestern.edu; Fax: (847) 491-4455

Authors

Chang-Mo Kang — *Department of Electrical and Computer Engineering, Northwestern University, Evanston, Illinois 60208-2900, United States;* ⓞ orcid.org/0000-0003-0060-2434

Simone Bianconi — *Department of Electrical and Computer Engineering, Northwestern University, Evanston, Illinois 60208-2900, United States;* ⓞ orcid.org/0000-0002-3828-6513

Travis Hamilton — *Department of Electrical and Computer Engineering, Northwestern University, Evanston, Illinois 60208-2900, United States*

Jacob Rabinowitz — *Department of Physics & Astronomy and CIERA, Northwestern University, Evanston, Illinois 60208-2900, United States;* ⓞ orcid.org/0000-0002-2930-5655

Skyler Wheaton — *Department of Electrical and Computer Engineering, Northwestern University, Evanston, Illinois 60208-2900, United States*

Lining Liu — *Department of Electrical and Computer Engineering, Northwestern University, Evanston, Illinois 60208-2900, United States*

Melville Ulmer — *Department of Physics & Astronomy and CIERA, Northwestern University, Evanston, Illinois 60208-2900, United States*

Complete contact information is available at:
https://pubs.acs.org/10.1021/acsaelm.2c00109

Author Contributions

C.-M.K. invented the main idea of this study and realized the FPA device. C.-M.K. fabricated the samples for the measurement of transmittance and focal length. S.B. installed the setup for measuring the focal length of MLAs, and S.B. and C.-M.K. measured the focal length and the broad-band transmittance of MLAs. T.H. plotted the 3D focal length, and T.H. and C.-M.K. did the FDTD simulation of MLAs. J.R. did the camera measurement and wrote the measurement part in the Experimental Methods section. S.W. installed the transmittance setup with the focused beam, and S.W. and C-.M.K measured the transmittance. L.L. and C.-M.K. did the flip-chip bonding. C.-M.K. put together all data and configured the figure set. C.-M.K. and S.B. wrote the manuscript. H.M. supervised the entire work and revised this manuscript. All authors discussed the results.

Notes

The authors declare no competing financial interest.

■ REFERENCES

(1) Jovanovic, N.; Martinache, F.; Guyon, O.; Clergeon, C.; Singh, G.; Kudo, T.; Garrel, V.; Newman, K.; Doughty, D.; Lozi, J.; Males, J.; Minowa, Y.; Hayano, Y.; Takato, N.; Morino, J.; Kuhn, J.; Serabyn, E.; Norris, B.; Tuthill, P.; Schworer, G.; Stewart, P.; Close, L.; Huby, E.; Perrin, G.; Lacour, S.; Gauchet, L.; Vievard, S.; Murakami, N.; Oshiyama, F.; Baba, N.; Matsuo, T.; Nishikawa, J.; Tamura, M.; Lai, O.; Marchis, F.; Duchene, G.; Kotani, T.; Woillez, J. The Subaru Coronagraphic Extreme Adaptive Optics System: Enabling High-Contrast Imaging on Solar-System Scales. *Publ. Astron. Soc. Pac.* **2015**, *127*, 890−910.
(2) Hong, G.; Lee, J. C.; Robinson, J. T.; Raaz, U.; Xie, L.; Huang, N. F.; Cooke, J. P.; Dai, H. Multifunctional in vivo vascular imaging using near-infrared II fluorescence. *Nat. Med.* **2012**, *18*, 1841−1846.
(3) Zhong, L.; Li, X.; Zhu, M.; Hu, Z.; Chen, F. Improved Intra-Pixel Sensitivity Characterization Based on Diffusion and Coupling Model for Infrared Focal Plane Array Photodetector. *Sensors* **2021**, *21*, 8195.
(4) Guyon, O.; Martinache, F.; Cady, E.; Belikov, R.; Kunjithapatham, B.; Wilson, D.; Clergeon, C.; Mateen, M. How ELTs will acquire the first spectra of rocky habitable planets. *SPIE Proc.* **2012**, *8447*, No. 84471X.
(5) Hinz, P.; Codona, J.; Guyon, O.; Hoffmann, W.; Skemer, A.; Hora, J.; Tolls, V.; Boss, A.; Weinberger, A.; Arbo, P.; Connors, T.; Durney, O.; McMahon, T.; Montoya, M.; Vaitheeswaran, V. TIGER: A High Contrast infrared imager for the Giant Magellan Telescope. *SPIE Proc.* **2012**, *8446*, No. 84461P.
(6) Strausbaugh, R.; Jackson, R.; Butler, N. Night Vision for Small Telescopes. *Publ. Astron. Soc. Pac.* **2018**, *130*, No. 095001.
(7) Joshi, A.; Stevens, J.; Kononenko, A.; Blackwell, J. Ultra-Low Noise High Frame Rate ROIC for Visible and Infrared Focal Plane Arrays. *SPIE Proc.* **2004**, *5499*, 228−239.
(8) Fathipour, V.; Bonakdar, A.; Mohseni, H. Advances on Sensitive Electron-Injection Based Cameras for Low-Flux, Short-Wave Infrared Applications. *Front. Mater.* **2016**, *3*, 33.

(9) Bianconi, S.; Mohseni, H. Recent advances in infrared imagers: toward thermodynamic and quantum limits of photon sensitivity. *Rep. Prog. Phys.* **2020**, *83*, No. 044101.
(10) Rezaei, M.; Park, M.-S.; Tan, C. L.; Mohseni, H. Sensitivity Limit of Nanoscale Phototransistors. *IEEE Electron Device Lett.* **2017**, *38*, 1051−1054.
(11) Soibel, A.; Keo, S. A.; Fisher, A.; Hill, C. J.; Luong, E.; Ting, D. Z.; Gunapala, S. D.; Lubyshev, D.; Qiu, Y.; Fastenau, J. M.; Liu, A. W. K. High operating temperature nBn detector with monolithically integrated microlens. *Appl. Phys. Lett.* **2018**, *112*, No. 041105.
(12) Zhang, S.; Soibel, A.; Keo, S. A.; Wilson, D.; Rafol, S. B.; Ting, D. Z.; She, A.; Gunapala, S. D.; Capasso, F. Solid-immersion metalenses for infrared focal plane arrays. *Appl. Phys. Lett.* **2018**, *113*, No. 111104.
(13) Rogalski, A.; Martyniuk, P.; Kopytko, M. Challenges of small-pixel infrared detectors: a review. *Rep. Prog. Phys.* **2016**, *79*, No. 046501.
(14) Ma, J.; Masoodian, S.; Starkey, D. A.; Fossum, E. R. Photon-number-resolving megapixel image sensor at room temperature without avalanche gain. *Optica* **2017**, *4*, 1474−1481.
(15) Rezaei, M.; Bianconi, S.; Lauhon, L. J.; Mohseni, H. A New Approach to Designing High-Sensitivity Low-Dimensional Photodetectors. *Nano Lett.* **2021**, *21*, 9838−9844.
(16) *Infrared Detectors*; 2nd; Rogalski, A., Ed.; CRC Press: Boca Raton, FL, 2010.
(17) Adinolfi, V.; Sargent, E. H. Photovoltage field-effect transistors. *Nature* **2017**, *542*, 324−327.
(18) Ko, W. S.; Bhattacharya, I.; Tran, T.-T. D.; Ng, K. W.; Gerke, S. A.; Chang-Hasnain, C. Ultrahigh Responsivity-Bandwidth Product in a Compact InP Nanopillar Phototransistor Directly Grown on Silicon. *Sci. Rep.* **2016**, *6*, No. 33368.
(19) Konstantatos, G.; Badioli, M.; Gaudreau, L.; Osmond, J.; Bernechea, M.; Arquer, F. P. G.; Gatti, F.; Koppens, F. H. L. Hybrid graphene−quantum dot phototransistors with ultrahigh gain. *Nat. Nanotechnol.* **2012**, *7*, 363−368.
(20) Ackerman, M. M.; Tang, X.; Guyot-Sionnest, P. Fast and Sensitive Colloidal Quantum Dot Mid-Wave Infrared Photodetectors. *ACS Nano* **2018**, *12*, 7264−7271.
(21) Hu, Y.; Zhou, J.; Yeh, P.-H.; Li, Z.; Wei, T.-Y.; Wang, Z. L. Supersensitive, Fast-Response Nanowire Sensors by Using Schottky Contacts. *Adv. Mater.* **2010**, *22*, 3327−3332.
(22) Rezaei, M.; Park, M.-S.; Rabinowitz, C.; Tan, C. L.; Wheaton, S.; Ulmer, M.; Mohseni, H. InGaAs based heterojunction phototransistors: Viable solution for high-speed and low-noise short wave infrared imaging. *Appl. Phys. Lett.* **2019**, *114*, No. 161101.
(23) Yamamoto, K. Image sensor having micro-lens array separated with trench structures and method of making. US patent US6,933,167 B2, Aug. 23, 2005.
(24) Wu, T.-C.; Y Microlens designs for CMOS image sensors. US patent, US7,196,388 B2, Mar. 27, 2007.
(25) Rothman, J.; Bleuet, P.; Abergel, J.; Gout, S.; Lasfargues, G.; Mathieu, L.; Nicolas, J.-A.; Rostaing, J.-P.; Huet, S.; Castelein, P.; Aubaret, K.; Saint-Pé, O. HgCdTe APDs detector developments at CEA/Leti for atmospheric LIDAR and Free space optical communications. *SPIE Proc.* **2018**, *11180*, No. 111803S.
(26) Piotrowski, J.; Rogalski, A. Uncooled long wavelength infrared photon detectors. *Infrared Phys. Technol.* **2004**, *46*, 115−131.
(27) He, M.; Yuan, X.; Moh, K. J.; Bu, J.; Yi, X.-J. Monolithically integrated refractive microlens array to improve imaging quality of an infrared focal plane array. *Opt. Eng.* **2004**, *43*, 2589−2594.
(28) Thibault, S. Consumer Electronic Optics: How Small a Lens Can Be Using Metasurfaces. *SPIE Proc.* **2019**, *9192*, No. 1110406.
(29) Wang, S.; Wu, P. C.; Su, V.-C.; Lai, Y.-C.; Chu, C. H.; Chen, J.-W.; Lu, S.-H.; Chen, J.; Xu, B.; Kuan, C.-H.; Li, T.; Zhu, S.; Tsai, D. P. Broadband achromatic optical metasurface devices. *Nat. Commun.* **2017**, *8*, No. 187.
(30) Presutti, F.; Monticone, F. Focusing on bandwidth: achromatic metalens limits. *Optica* **2020**, *7*, 624−631.

(31) Driggers, R. G.; Vollmerhausen, R.; Reynolds, J. P.; Fanning, J.; Holst, G. C. Infrared detector size: how low should you go? *Opt. Eng.* **2012**, *51*, No. 063202.

(32) Bagdahn, J.; Petzold, M. *Wafer Bonding: Applications and Technology* Alexe, M.; Gosele, U., Eds.; Springer, 2004, Chapter 14.

(33) Gurnett, K.; Adams, T. Ultra-thin semiconductor wafer applications and processes. *III-Vs Review* **2006**, *19*, 38−40.

(34) Tsutsumi, T.; Kosugi, T.; Matsuzaki, H. Wafer-level Backside Process Technology for Forming High-density Vias and Backside Metal Patterning for 50-μm-thick InP Substrate. *CS MANTECH Conference* **2013**, 55−58.

(35) Nussbaum, Ph.; Volkel, R.; Herzig, H. P.; Eisner, M.; Haselbeck, S. Design, fabrication and testing of microlens arrays for sensors and microsystems. *Pure Appl. Opt.* **1997**, *6*, 617−636.

(36) Allouti, N.; Chevalier, P.; Bérard-Bergery, S.; Rousset, V.; Mortini, B.; Quéméré, P.; Tomaso, F.; Coquand, R. Grayscale lithography process study for sub 5μm microlens patterns. *Proc. SPIE* **2019**, *10958*, No. 1095809.

K